Layered Compounds

Deutsche Ausgabe: DOI: 10.1002/ange.201510029
Internationale Ausgabe: DOI: 10.1002/anie.201510029

Low-Temperature Solution Synthesis of Few-Layer 1T′-$MoTe_2$ Nanostructures Exhibiting Lattice Compression

Yifan Sun, Yuanxi Wang, Du Sun, Bruno R. Carvalho, Carlos G. Read, Chia-hui Lee, Zhong Lin, Kazunori Fujisawa, Joshua A. Robinson, Vincent H. Crespi, Mauricio Terrones, and Raymond E. Schaak**

Abstract: *Molybdenum ditelluride, $MoTe_2$, is emerging as an important transition-metal dichalcogenide (TMD) material because of its favorable properties relative to other TMDs. The 1T′ polymorph of $MoTe_2$ is particularly interesting because it is semimetallic with bands that overlap near the Fermi level, but semiconducting 2H-$MoTe_2$ is more stable and therefore more accessible synthetically. Metastable 1T′-$MoTe_2$ forms directly in solution at 300 °C as uniform colloidal nanostructures that consist of few-layer nanosheets, which appear to exhibit an approx. 1 % lateral lattice compression relative to the bulk analogue. Density functional theory calculations suggest that small grain sizes and polycrystallinity stabilize the 1T′ phase in the $MoTe_2$ nanostructures and suppress its transformation back to the more stable 2H polymorph through grain boundary pinning. Raman spectra of the 1T′-$MoTe_2$ nanostructures exhibit a laser energy dependence, which could be caused by electronic transitions.*

Transition-metal dichalcogenides (TMDs) of the Group 6 elements, including MoS_2, $MoSe_2$, WS_2, and WSe_2, are layered van der Waals solids having fascinating properties that depend sensitively on the thickness and stacking registry of the metal–chalcogen slabs that comprise them, as well as on the crystal symmetry, coordination environment, and lattice strain.[1–3] As a result, monolayer and few-layer TMD nanosheets have emerged as important and tunable materials for new applications in catalysis,[4] energy conversion and storage,[5,6] photovoltaics,[7] biosensing,[8] and electronic and optoelectronic devices.[9–11] $MoTe_2$ has recently become a particularly interesting TMD target because of its small band gap, low thermal conductivity, and high Seebeck coefficient relative to its sulfur and selenium analogues,[12] as well as reports of superconductivity[13] and possible new capabilities in valleytronics.[14] However, accessing two-dimensional (2D) sheets of $MoTe_2$ is more challenging than for MoS_2 and $MoSe_2$ because of synthetic issues with precursors and products, including oxidation,[15] volatility,[16] thermal instability,[17] and phase targeting.[18] Solution-dispersible $MoTe_2$ nanostructures reported previously required exfoliation of bulk powders[19] or produced irregular particle mixtures.[20]

The most stable polymorph of $MoTe_2$ is the hexagonal 2H phase, which has trigonal prismatic coordination and is semiconducting with a band gap of about 1.0 eV.[21] The 1T′ phase, which is monoclinic and has a distorted octahedral coordination environment for Mo that contains in-plane metal-metal bonds, is stable at higher temperatures than the 2H polymorph and is semimetallic with bands that overlap near the Fermi level.[17,22] 2H-$MoTe_2$ therefore is more synthetically accessible than metastable 1T′-$MoTe_2$, although there is only a small energy difference between the 2H and 1T′ polymorphs.[23] This near-degeneracy is useful for some applications of $MoTe_2$, such as phase-change memories and the facile creation of ohmic heterophase homojunctions between 2H- and 1T′-$MoTe_2$ via laser-induced patterning.[24] However, the small energy difference between 2H- and 1T′-$MoTe_2$ makes it challenging to selectively target one polymorph, and subtly different synthetic parameters can lead unpredictably to the formation of one vs. the other.[18] Herein, we report a low-temperature solution-phase synthesis that leads directly to the formation of the higher-temperature 1T′ polymorph of $MoTe_2$. 1T′-$MoTe_2$ forms as uniform flower-like nanostructures comprised of few-layer nanosheets that appear to exhibit an approx. 1 % lateral lattice compression relative to the bulk analogue, and density functional theory (DFT) calculations suggest that transformation back to the more stable 2H polymorph is suppressed through grain boundary pinning. Furthermore, we discuss an observed dependence of the 1T′-$MoTe_2$ Raman spectra on the laser energy.

1T′-$MoTe_2$ was synthesized by injecting a solution of $MoCl_5$ in oleic acid dropwise into a mixture of trioctylphosphine (TOP), trioctylphosphine telluride (TOP-Te), oleylamine, and hexamethyldisilazane (HMDS) at 300 °C, as

[*] Y. Sun, D. Sun, C. G. Read, Prof. V. H. Crespi, Prof. M. Terrones, Prof. R. E. Schaak
Department of Chemistry, The Pennsylvania State University
University Park, PA 16802 (USA)
E-mail: mut11@psu.edu
res20@psu.edu
Y. Wang, B. R. Carvalho, Z. Lin, K. Fujisawa, Prof. V. H. Crespi, Prof. M. Terrones
Department of Physics, The Pennsylvania State University
University Park, PA 16802 (USA)
C. Lee, Prof. J. A. Robinson, Prof. M. Terrones
Department of Materials Science and Engineering
The Pennsylvania State University
University Park, PA 16802 (USA)
Y. Wang, B. R. Carvalho, C. Lee, Z. Lin, Prof. J. A. Robinson, Prof. V. H. Crespi, Prof. M. Terrones, Prof. R. E. Schaak
Center for 2-Dimensional and Layered Materials
The Pennsylvania State University
University Park, PA 16802 (USA)
B. R. Carvalho
Departamento de Física, Universidade Federal de Minas Gerais
Belo Horizonte, Minas Gerais, 30123-970 (Brazil)

Supporting information for this article is available on the WWW under http://dx.doi.org/10.1002/anie.201510029.

described in the Supporting Information. It is conjectured that $MoCl_5$ reacts with oleic acid to form a molybdenum oleate complex[25,26] and that oleylamine provides a reducing atmosphere,[27,28] ultimately leading to the formation of $MoTe_2$. Control experiments indicate that HMDS is required to produce crystalline, uniform $MoTe_2$ nanostructures in high yield. After washing and centrifugation, the black-colored product was dispersed in ethanol and stored under argon. The $MoTe_2$ product oxidizes and becomes amorphous when exposed to air for several hours, as indicated by powder X-ray diffraction (XRD; Supporting Information, Figure S1) and X-ray photoelectron spectroscopy (XPS) data (Supporting Information, Figure S2); a similar instability under ambient conditions for mechanically exfoliated $MoTe_2$ grown by chemical vapor transport has been reported previously.[29] For the $MoTe_2$ nanostructures produced herein, storage in ethanol and under argon helps to mitigate the degradation process, although surface oxidation cannot be completely prevented. Figure 1 a,b and the Supporting Information, Figure S3 show transmission electron microscopy (TEM) images of the $MoTe_2$ product, which consists of flower-like nanostructures having diameters that range from 100–150 nm. The nanoflowers contain aggregates of few-layer nanosheets that emanate from a central core, as has been observed previously for $MoSe_2$[30] and other solution-synthesized TMD nanostructures.[5,31] Energy-dispersive X-ray spectroscopy (EDS) data, shown in the Supporting Information, Figure S3, confirms the 1:2 ratio of Mo to Te, and comparison of the selected area electron diffraction (SAED) pattern with the simulated diffraction pattern, suggests the formation of 1T′-$MoTe_2$ (Figure 1 c).

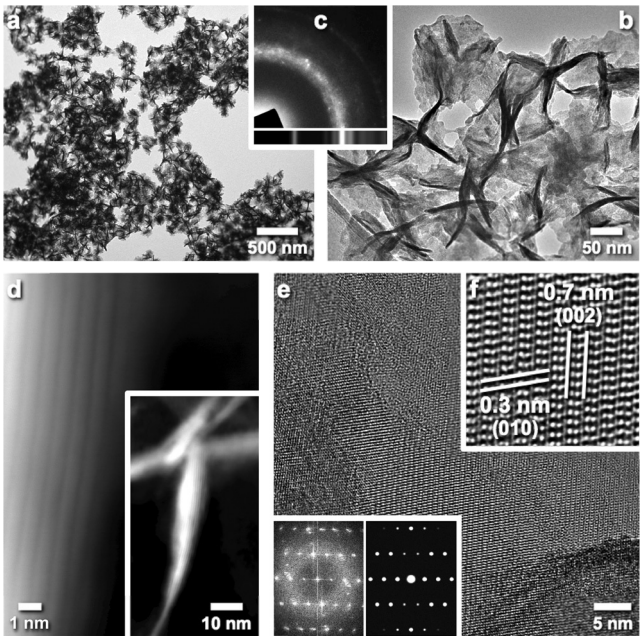

Figure 1. Representative a) low- and b) high-magnification TEM images of 1T′-$MoTe_2$ nanostructures. The corresponding SAED pattern is shown in (c), along with a simulated pattern at the bottom for comparison. d) High- and low-magnification HAADF-STEM images of curled few-layer nanosheets showing the (002) interlayer spacing. e) HRTEM image showing the polycrystalline nature. An enlarged HRTEM image of the (100) plane is shown in (f). The inset in (e) shows the FFT of the (100) plane in (f), along with the simulated [100] diffraction pattern.

High-resolution TEM (HRTEM) images (Figure 1 d,e; Supporting Information, Figure S3) reveal multiple crystal facets owing to the curled and aggregated nature of the nanosheets that protrude from the central core. The HAADF-STEM image in the inset of Figure 1 d shows a side view of a curled-up few-layer nanosheet. The observed lattice spacing of 0.7 nm, shown in the main panel of Figure 1 d, matches well with that expected for the (002) plane of 1T′-$MoTe_2$. The HRTEM image in Figure 1 e shows that the 1T′-$MoTe_2$ nanoflowers are comprised of crystalline domains that are approx. 10 nm in diameter with observed lattice spacings of 0.3 nm and 0.7 nm, which correspond well to the expected values for the (010) and (002) planes of 1T′-$MoTe_2$, respectively. As shown in the inset to Figure 1 e, the simulated diffraction pattern for the [100] projection of 1T′-$MoTe_2$ matches well, both quantitatively and qualitatively, with the fast Fourier transform (FFT) of the HRTEM image in Figure 1 f.

Powder XRD data further confirm the formation of 1T′-$MoTe_2$ and also provide important insights into the unique structural features of the few-layer nanosheets. The experimental powder XRD pattern for the 1T′-$MoTe_2$ nanostructures, along with simulated patterns for 2H-$MoTe_2$, 1T′-$MoTe_2$, and T_d-$MoTe_2$ for comparison are shown in the Supporting Information, Figure S1. The simulated XRD pattern for 2H-$MoTe_2$ does not match the experimental XRD pattern. The simulated XRD pattern for T_d-$MoTe_2$, which is a less-common higher-symmetry orthorhombic variant of monoclinic 1T′-$MoTe_2$,[32] also does not satisfactorily account for all peaks and peak positions. 1T′-$MoTe_2$ appears to be the best match, but the peak positions of the database pattern diverge measurably from those of the experimental pattern, especially at higher 2θ values.

Figure 2 shows a whole-pattern profile fit of the experimental XRD data using 1T′-$MoTe_2$ as the initial model. Because of the low-symmetry monoclinic crystal structure of 1T′-$MoTe_2$, the large number of closely spaced peaks, and a lack of peak-to-peak resolution owing to the peak broadening that results from the nanoscale domains, only the a, b, c, and β lattice parameters were refined while all other parameters and variables remained fixed. The primary goal of the whole-pattern fit was to ascertain how the lattice parameters would have to change to best match the experimental data. The refinement of the 1T′-$MoTe_2$ nanostructures reproducibly converged to approximate lattice constants of $a = 6.25$, $b = 3.42$, $c = 13.79$ Å, and $\beta = 93.9°$. The value of β for bulk 1T′-$MoTe_2$ is 93.96°,[33] which matches that generated by the refinement. All of the other lattice constants decreased by 0.5–1.3 %, suggesting that the few-layer nanosheets that comprise the 1T′-$MoTe_2$ nanostructures exhibit a slight compressive lattice strain. Specifically, bulk 1T′-$MoTe_2$ (PDF no. 04–007–1140) has $a = 6.33$, $b = 3.47$, and $c = 13.86$ Å,[33] while the lattice constants for the 1T′-$MoTe_2$ nanostructures are −1.26 %, −1.30 %, and −0.51 % smaller,

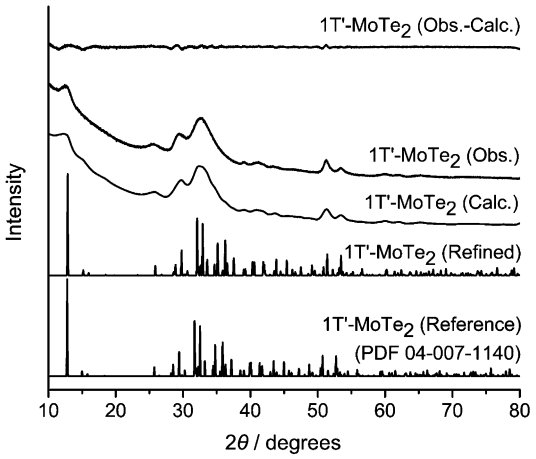

Figure 2. Powder XRD patterns, showing the experimental (observed) data for the 1T′-$MoTe_2$ nanostructures, the refined (calculated) XRD pattern, and the difference curve (observed−calculated). Reference patterns for 1T′-$MoTe_2$ (PDF card no. 04-007-1140) and 1T′-$MoTe_2$ incorporating the refined lattice constants after refinement are also shown.

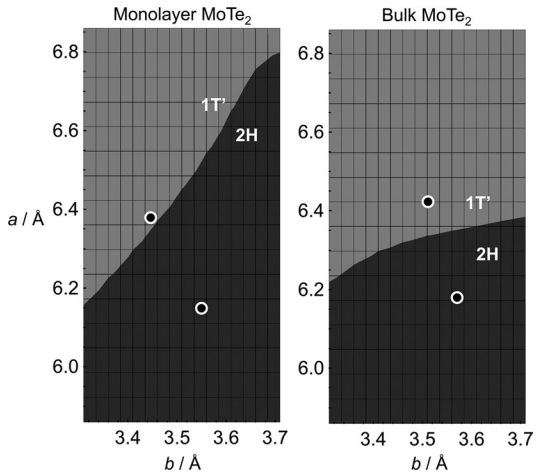

Figure 3. Phase diagrams of monolayer (left) and bulk (right) $MoTe_2$. The 1T′ phase is more energetically favorable in the lighter gray region, and the 2H phase is more energetically favorable in the darker gray region. The black dots outlined in white indicate the energy minimum for each phase.

respectively. Even with the low-symmetry crystal structure and broad peaks, the fit to the 1T′-$MoTe_2$ model having the refined lattice constants matches significantly better to the experimental data than the bulk 1T′-$MoTe_2$ data. While we cannot rule out the possibility that the $MoTe_2$ nanoflowers instead form the closely-related T_d polymorph, several factors suggest that 1T′-$MoTe_2$ is the most appropriate assignment at this stage, including the better match between the calculated and observed XRD peak positions, the known prevalence of 1T′-$MoTe_2$ relative to T_d-$MoTe_2$, and the small energy difference between 1T′-$MoTe_2$ and 2H-$MoTe_2$.

Obtaining the metastable 1T′-$MoTe_2$ phase rather than the more stable 2H polymorph is interesting, especially since the 1T′-$MoTe_2$ nanoflowers form directly at 300 °C, at which the 2H phase should be preferred. Calculations have shown that the energy difference between the 1T′ and 2H phases is smaller for ditellurides than it is for disulfides and diselenides, approaching only 35 meV per $MoTe_2$ unit.[18] Furthermore, organic ligands and solvents can modify the surface energy and further lower the energy barrier for forming 1T′-$MoTe_2$ rather than the 2H polymorph, as predicted computationally[34] and also as observed in the colloidal synthesis of 1T- and 2H-WS_2 nanosheets.[26] Additionally, among the Mo- and W-dichalcogenides, $MoTe_2$ is most amenable to phase transformation under lattice strain.[23] Indeed, a recent study proposed that 1T′-$MoTe_2$ is more stable than 2H-$MoTe_2$ under tensile strain, and this can be achieved in gas-phase synthesis by tuning the amount of Te.[35] Collectively, these previous experimental observations and computational predictions help to rationalize our observed formation of lattice-compressed 1T′-$MoTe_2$ when synthesized as few-layer nanosheet architectures at low temperatures in solution.

It is also interesting that the 1T′-$MoTe_2$ nanostructures do not transform back to the 2H polymorph. Figure 3 and the Supporting Information, Figure S4 show the total energy plotted as a function of the lateral lattice constants a and b, producing a 1T′/2H phase diagram for bulk and monolayer $MoTe_2$, as calculated using density functional theory (DFT; see the Supporting Information for details). The c axes are fixed at the experimental values for each phase while the a and b lattice constants vary from 5.86–6.86 Å and 3.31–3.71 Å, respectively. Although the energy minimum for the 2H phase is lower than that of 1T′, the difference of only 13 and 42 meV per $MoTe_2$ unit for bulk and monolayer systems, respectively, is comparable to room temperature thermal energies, thus opening up the possibility for phase accessibility. The calculations also reveal that a transition from 1T′-$MoTe_2$ to 2H-$MoTe_2$ requires changing both the a and b lattice constants significantly. Because of the polycrystalline nature of the nanosheets and the small 8–10 nm grain sizes, as shown in Figure 1 and the Supporting Information, Figure S3, simultaneous changes of the a and b lattice constants could be mechanically disfavored. Given an initial 1T′ structure with lattice constants at the equilibrium values, the nucleation of the phase transition from 1T′ to 2H is made more difficult by mechanical pinning at grain boundaries. Therefore, the 1T′ structure could be locked in by a collective elastic-deformation barrier against the transformation into the more stable 2H polymorph. DFT calculations with the lattice parameters of the 2H and 1T′ phases both fixed at the equilibrium values of the 1T′ phase reveal that 1T′-$MoTe_2$ is indeed preferable by 25 meV per $MoTe_2$ unit for bulk systems and 5 meV for monolayer systems. This suggests that small grain sizes and polycrystallinity may effectively stabilize the metastable 1T′ phase in the $MoTe_2$ nanoflowers.

Figure 4 shows Raman spectra of the 1T′-$MoTe_2$ nanoflowers obtained with 2.54 eV (488 nm), 2.41 eV (514.5 nm), and 1.92 eV (647.1 nm) laser energies. Considering the instability of $MoTe_2$ under ambient conditions and to avoid heating effects and sample damage, we performed laser power dependence measurements from 4 to 65 μW for each wavelength, as shown in the Supporting Information, Fig-

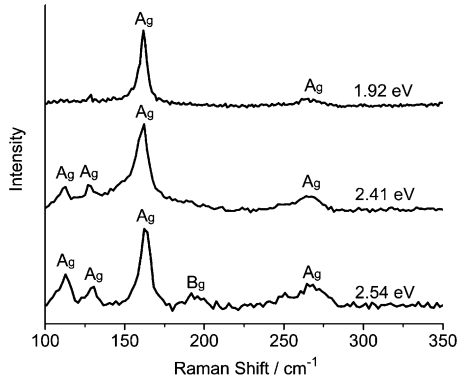

Figure 4. Raman spectra of the as-prepared 1T′-$MoTe_2$ nanostructures for excitation energies of 1.92 eV, 2.41 eV, and 2.54 eV. The spectra are normalized to the intensity of the A_g peak at 162 cm^{-1}. For clarity, the Raman modes are labeled according to bulk notation.

ure S5. The Raman spectra at laser energies of 2.41 eV and 2.54 eV show peaks corresponding to A_g modes, situated at 113 cm^{-1}, 130 cm^{-1}, 162 cm^{-1} and 264 cm^{-1}; this confirms the monoclinic phase of $MoTe_2$ and is in good agreement with our first-principles calculations (Supporting Information, Figures S6, S7). Furthermore, a peak related to the B_g mode is observed near 190 cm^{-1} at a 2.54 eV laser energy, as previously reported by Park et al.[35] Notably, two peaks below 150 cm^{-1} are observed at 2.41 and 2.54 eV laser energies, but not at 1.92 eV, suggesting a possible electronic resonance condition. Guo et al. have reported several features associated with a double-resonant Raman process at the *M* point in mono- and few-layer 2H-$MoTe_2$.[36] Although the Raman spectra of 1T′-$MoTe_2$ have recently been studied,[17,18] further calculations and measurements under different resonance conditions must be performed to gain a better understanding of these observations.

In conclusion, 1T′-$MoTe_2$ nanoflowers have been synthesized using a low-temperature solution method. The compressive lattice strain and polycrystalline nature of the few-layer nanosheet flower-like architectures contribute to the formation of the 1T′ phase, which exhibits wavelength-dependent Raman spectra. The ability to access metastable and lattice-compressed TMD polymorphs using colloidal synthesis techniques complements more traditional gas-phase fabrication techniques, thus opening the door to larger-quantity samples that are not confined to a substrate, as well as targeted phase formation using lower temperatures and different reagents.

Acknowledgements

Y.S., D.S., and R.E.S. (synthesis and materials characterization) were supported by the U.S. National Science Foundation Grant No. DMR-1305564. Y.W., V.H.C., and M.T. acknowledge support from U.S. Army Research Office MURI grant W911NF-11-1-0362. B.R.C. acknowledges financial support from Brazilian agency FAPEMIG. J.A.R. acknowledges support from the National Science Foundation CAREER Award 1453924. J.A.R., V.H.C., M.T., and R.E.S. also acknowledge the Center for 2-Dimensional and Layered Materials at the Pennsylvania State University. Electron microscopy, XPS, and XRD were performed at the Penn State Microscopy and Cytometry Facility (University Park, PA) and at the Materials Characterization Lab of the Penn State Materials Research Institute. We thank Nicole Wonderling and Gino Tambourine for help with XRD refinements and Josh Stapleton for optical measurements.

Keywords: chalcogenides · layered compounds · metastable compounds · nanostructures · transition-metal dichalcogenides

How to cite: *Angew. Chem. Int. Ed.* **2016**, *55*, 2830–2834
Angew. Chem. **2016**, *128*, 2880–2884

[1] M. Chhowalla, H. S. Shin, G. Eda, L.-J. Li, K. P. Loh, H. Zhang, *Nat. Chem.* **2013**, *5*, 263–275.
[2] D. Voiry, A. Mohite, M. Chhowalla, *Chem. Soc. Rev.* **2015**, *44*, 2702–2712.
[3] R. Lv, J. A. Robinson, R. E. Schaak, D. Sun, Y. Sun, T. E. Mallouk, M. Terrones, *Acc. Chem. Res.* **2015**, *48*, 56–64.
[4] Y. Li, H. Wang, L. Xie, Y. Liang, G. Hong, H. Dai, *J. Am. Chem. Soc.* **2011**, *133*, 7296–7299.
[5] Z. Hu, L. Wang, K. Zhang, J. Wang, F. Cheng, Z. Tao, J. Chen, *Angew. Chem. Int. Ed.* **2014**, *53*, 12794–12798; *Angew. Chem.* **2014**, *126*, 13008–13012.
[6] W. Wu, L. Wang, Y. Li, F. Zhang, L. Lin, S. Niu, D. Chenet, X. Zhang, Y. Hao, T. F. Heinz, J. Hone, Z. L. Wang, *Nature* **2014**, *514*, 470–474.
[7] M. Bernardi, M. Palummo, J. C. Grossman, *Nano Lett.* **2013**, *13*, 3664–3670.
[8] K. Kalantar-zadeh, J. Z. Ou, T. Daeneke, M. S. Strano, M. Pumera, S. L. Gras, *Adv. Funct. Mater.* **2015**, *25*, 5086–5099.
[9] B. Radisavljevic, A. Radenovic, J. Brivio, V. Giacometti, A. Kis, *Nat. Nanotechnol.* **2011**, *6*, 147–150.
[10] A. Splendiani, L. Sun, Y. Zhang, T. Li, J. Kim, C.-Y. Chim, G. Galli, F. Wang, *Nano Lett.* **2010**, *10*, 1271–1275.
[11] N. R. Pradhan, D. Rhodes, S. Feng, Y. Xin, S. Memaran, B.-H. Moon, H. Terrones, M. Terrones, L. Balicas, *ACS Nano* **2014**, *8*, 5911–5920.
[12] S. Balendhran, S. Walia, H. Nili, J. Z. Ou, S. Zhuiykov, R. B. Kaner, S. Sriram, M. Bhaskaran, K. Kalantar-Zadeh, *Adv. Funct. Mater.* **2013**, *23*, 3952–3970.
[13] Y. Qi, P. G. Naumov, M. N. Ali, C. R. Rajamathi, O. Barkalov, Y. Sun, C. Shekhar, S.-C. Wu, V. Süß, M. Schmidt, E. Pippel, P. Werner, R. Hillebrand, T. Förster, E. Kampertt, W. Schnelle, S. Parkin, R. J. Cava, C. Felser, B. Yan, S. A. Medvedev, **2015**, arXiv: 1508.03502 [cond-mat.mtrl-sci].
[14] D. Xiao, G.-B. Liu, W. Feng, X. Xu, W. Yao, *Phys. Rev. Lett.* **2012**, *108*, 196802.
[15] B. Chen, H. Sahin, A. Suslu, L. Ding, M. I. Bertoni, F. M. Peeters, S. Tongay, *ACS Nano* **2015**, *9*, 5326–5332.
[16] L. Zhou, K. Xu, A. Zubair, A. D. Liao, W. Fang, F. Ouyang, Y.-H. Lee, K. Ueno, R. Saito, T. Palacios, J. Kong, M. S. Dresselhaus, *J. Am. Chem. Soc.* **2015**, *137*, 11892–11895.
[17] M. Kan, H. G. Nam, Y. H. Lee, Q. Sun, *Phys. Chem. Chem. Phys.* **2015**, *17*, 14866–14871.
[18] D. H. Keum, S. Cho, J. H. Kim, D.-H. Choe, H.-J. Sung, M. Kan, H. Kang, J.-Y. Hwang, S. W. Kim, H. Yang, K. J. Chang, Y. H. Lee, *Nat. Phys.* **2015**, *11*, 482–486.
[19] G. Cunningham, M. Lotya, C. S. Cucinotta, S. Sanvito, S. D. Bergin, R. Menzel, M. S. P. Shafer, J. N. Coleman, *ACS Nano* **2012**, *6*, 3468–3480.

[20] a) L. Qiu, V. G. Pol. , Y. Wei, A. Gedanken, *J. Mater. Chem.* **2003**, *13*, 2985 – 2988; b) L. Qiu, Y. Wei, V. G. Pol, A. Gedanken, *Inorg. Chem.* **2004**, *43*, 6061 – 6066.
[21] Q. H. Wang, K. Kalantar-Zadeh, A. Kis, J. N. Coleman, M. S. Strano, *Nat. Nanotechnol.* **2012**, *7*, 699 – 712.
[22] M. B. Vellinga, R. de Jonge, C. Haas, *J. Solid State Chem.* **1970**, *2*, 299 – 302.
[23] K.-A. N. Duerloo, Y. Li, E. J. Reed, *Nat. Commun.* **2014**, *5*, 4214.
[24] S. Cho, S. Kim, J. H. Kim, J. Zhao, J. Seok, D. H. Keum, J. Baik, D.-H. Choe, K. J. Chang, K. Suenaga, S. W. Kim, Y. H. Lee, H. Yang, *Science* **2015**, *349*, 625 – 628.
[25] W. Fu, F.-H. Du, J. Su, X.-H. Li, X. Wei, T.-N. Ye, K.-X. Wang, J.-S. Chen, *Sci. Rep.* **2014**, *4*, 4673.
[26] B. Mahler, V. Hoepfner, K. Liao, G. A. Ozin, *J. Am. Chem. Soc.* **2014**, *136*, 14121 – 14127.
[27] S. Jeong, D. Yoo, J. Jang, M. Kim, J. Cheon, *J. Am. Chem. Soc.* **2012**, *134*, 18233 – 18236.
[28] S. Mourdikoudis, L. M. Liz-marzán, *Chem. Mater.* **2013**, *25*, 1465 – 1476.
[29] C. Ruppert, O. B. Aslan, T. F. Heinz, *Nano Lett.* **2014**, *14*, 6231 – 6236.
[30] D. Sun, S. Feng, M. Terrones, R. E. Schaak, *Chem. Mater.* **2015**, *27*, 3167 – 3175.
[31] Y. Lu, X. Yao, J. Yin, G. Peng, P. Cui, X. Xu, *RSC Adv.* **2015**, *5*, 7938 – 7943.
[32] W. G. Dawson, D. W. Bullett, *J. Phys. C* **1987**, *20*, 6159 – 6174.
[33] B. E. Brown, *Acta Crystallogr.* **1966**, *20*, 268 – 274.
[34] W. Jung, S. Lee, D. Yoo, S. Jeong, P. Miró, A. Kuc, T. Heine, J. Cheon, *J. Am. Chem. Soc.* **2015**, *137*, 7266 – 7269.
[35] J. C. Park, S. J. Yun, H. Kim, J.-H. Park, S. H. Chae, S.-J. An, J.-G. Kim, S. M. Kim, K. K. Kim, Y. H. Lee, *ACS Nano* **2015**, *9*, 6548 – 6554.
[36] H. Guo, T. Yang, M. Yamamoto, L. Zhou, R. Ishikawa, K. Ueno, K. Tsukagoshi, Z. Zhang, M. S. Dresselhaus, R. Saito, *Phys. Rev. B* **2015**, *91*, 205415.

Received: October 27, 2015
Published online: January 25, 2016

